Regulating the generation of reactive oxygen species for photocatalytic oxidation by metalloporphyrinic covalent organic frameworks

Suleman Suleman [a], Xinyu Guan [a], Yi Zhang [a], Amir Waseem [b], Onder Metin [c], Zheng Meng [a],[*], Hai-Long Jiang [a],[*]

[a] Department of Chemistry, University of Science and Technology of China, Hefei, Anhui 230026, PR China
[b] Department of Chemistry, Quaid-i-Azam University, Islamabad 45320, I. R. Pakistan
[c] Department of Chemistry, College of Sciences, Koç University, Istanbul 34450, Turkey

ARTICLE INFO

ABSTRACT

Regulating the generation of reactive oxygen species (ROS) impacts the selectivity and activity of photocatalytic oxidation, but the frequently concurrent formation of different types of ROS makes this process rather challenging. This study demonstrates the regulated production of two important ROS, $^1O_2$ and $O_2^{\bullet-}$, using a covalent-organic framework (COF) array with three members, which are made up of metalloporphyrin cores with embedded center metal ions from d-block transition metals sequentially arranged in the periodic table. Due to the evolution of the electronic structures in this COF array, the production of $^1O_2$ and $O_2^{\bullet-}$ is controlled, which successively leads to distinct performance in photocatalytic aerobic oxidations. The electronic property study and density-functional theory (DFT) calculations revealed that the distinct excitonic behavior of three COFs in regulated $^1O_2$ and $O_2^{\bullet-}$ generation is rooted in their different band energy levels and O_2 adsorption ability. Our work presents an effective approach to the controlled production of ROS for improved photocatalytic performance.

1. Introduction

ROS, which is a big family consisting of superoxide radical ($O_2^{\bullet-}$), hydroxyl radical ($^\bullet OH$), and singlet oxygen ($^1O_2$), play critical roles in organic synthesis [1–3], wastewater treatment [4,5], and photodynamic therapy [6] due to their high reactivity and oxidizing ability [6–8]. Among different types of ROS, $^1O_2$ and $O_2^{\bullet-}$ are the two most significant ones in photocatalytic oxidation reaction systems, which can be generated via the interaction of photoactivated charge carriers with the surrounding oxygen. In ROS-involved photocatalytic reactions, different types of ROS participate in different reaction pathways, which successively affect the activity and selectivity of the reaction. Because of the dominant role of ROS in aerobic oxidation, effective control of ROS generation is crucial for the efficiency of photocatalytic oxidation. However, the regulated generation of ROS is challenging since different ROS are concurrently formed during the interaction between O_2 and photoactivated charge carriers from the photocatalysts [9,10], and the discrepancies in their activities, oxidation capacities, and mechanisms of production for these ROS would result in poor selectivity and activity for

photocatalysis [11].

To date, efficient catalytic systems for photocatalytic aerobic oxidation reactions usually rely on organic dyes [12], fullerene derivates [13], metal oxides [14,15], and semiconductor quantum dots [16]. However, these catalytic systems pose challenges for selective ROS formation as a variety of ROS can be initiated on their valence bands or conduction bands and therefore exhibit poor selectivity and easy photobleaching, which severely limits their potential applications. Furthermore, noble metals, including Pt, Au, and Ag, have been exploited for aerobic oxidations [17,18]. Still, they are expensive and not amendable for wide-scale use due to their scarcity. On top of that, polymers have also been employed for the aerobic oxidations [19–22]. However, the lack of well-organized structures in traditional polymers makes it challenging to craft and modify them with precision. This, in turn, poses difficulties in maintaining precise control over excitons and in establishing a clear link between excitonic effects and their associated properties. Especially for COFs, which is crystalline polymers with precise and tailorable structures offer an advantageous platform for investigating the relationship between structure and photocatalytic

activity through molecular-level structural regulation, holding great potential for advanced photocatalysis in ROS regulation.

Distinct from traditional aerobic photocatalyst systems, COFs, which are porous and crystalline framework materials with well-defined structures made by linking molecular building blocks with earth-abundant elements, have the potential to overcome the above shortcomings and realize selective ROS generation. *Firstly*, attributed to the flexibility in the choice of molecular building moieties and diversity in their chemical structures, these reticular materials can be engineered with suitable band energy levels, which are critical for light harvesting and consequent charge carrier formation and transfer processes [23]. *Secondly*, the open structure of COFs provides opportunities for reaction substrates to be accessible and, therefore, can maximize the activation substrates for achieving high activity [24,25]. *Thirdly*, COFs with well-defined and tunable structures at atomic precision can afford systematic chemical control over excitons, which allows the disclosure of a clear relationship profile between ROS effects and related properties [26]. In addition, the synthesis of new hydrazone-based metalloporphyrin COFs offers several advantages over metal-free hydrazone COFs, which have been reported for photocatalytic oxidation reactions [27]. Firstly, these advantages include tunable electronic structures based on central metal ions. Secondly, utilizing novel hydrazone-based metalloporphyrin COFs regulates conduction bands, facilitating precise control over specific ROS and enhancing selective activity.

With the above considerations in mind, herein we describe the design, synthesis, and characterization of three novel hydrazone-linked two-dimensional porphyrinic COFs (Fig. 1), named MPor-Dha (M = Co, Ni, and Cu), and their utilization for the effective regulation of $^1O_2$ and $O_2^{\bullet-}$ generation for a variety of photocatalytic oxidative organic reactions. Metalloporphyrins are chosen as the molecular building blocks for the construction of COFs due to their fascinating photophysical properties ascribed to their highly conjugated π-electron structure. In addition, the dependency of the photophysical properties of metalloporphyrins on central coordination metal ions, which metalating porphyrin macrocycles can handily control, will offer significant advantages for optimizing the oxygen activation process and tuning the O_2 adsorption affinity [25,28]. This array of COFs in our study has three members consisting of metalloporphyrin cores with embedded center metal ions from first-row transition metals. Since the electronic structures of the COFs evolve with the identity of center metals, the generation of $^1O_2$ and $O_2^{\bullet-}$ is tuned, consequently resulting in controllable activity and selectivity for the photocatalytic oxidation catalysis. Among all the three COFs, CoPor-Dha facilitates the dissociation of excitons into hot carriers for $O_2^{\bullet-}$-mediated photooxidation of phenylboronic acid

oxidation to phenol. Compared to CoPor-Dha, NiPor-Dha showed relatively weaker ability, yet stronger than CuPor-Dha, in the dissociation of excitons to hot carriers for $O_2^{\bullet-}$-mediated photooxidation of phenylboronic acid oxidation. CuPor-Dha preferentially promotes the conversion of triplet to singlet excitons, showing the highest activity for $^1O_2$-mediated thioanisole to sulfoxide. Our work provides an effective and modular strategy for the regulation of ROS to tune photocatalytic performance.

2. Experimental

2.1. Materials and equipment

All materials used were purchased from commercial vendors. Powder X-ray diffraction (PXRD) was collected using a Japan Rigaku Miniflex 600 rotation equipped with graphite monochromatized Cu Kα radiation (λ = 1.54 Å). The Shimadzu UV-3600 Plus was used to record all UV–vis absorption spectra from 300 and 800 nm. At a temperature of 77 K, nitrogen sorption isotherms were determined with a Micromeritics ASAP 2020 system. The samples were preactivated by exposure to supercritical carbon dioxide before the N_2 sorption measurement was carried out. Thermogravimetric analysis (TGA) was conducted using a TGA Q5000 integrated thermal analyzer at a heating rate of 10 °C per minute in air atmosphere. The metal contents were confirmed by inductively coupled plasma atomic emission spectrometry (ICP–AES) analyses performed on a Thermo Scientific iCAP 7400. The X-ray photoelectron spectroscopy (XPS) measurements were carried out with a high-performance Kratos Axis Supra + electron spectrometer and a monochromatized Al Kα (hν = 1486.6 eV) source. The products of the catalytic reaction were identified and analyzed with the help of a Shimadzu gas chromatograph (model GC-2010 Plus equipped with a 0.25 mm 30 m Rtx-5 capillary column). Xenon lamps with 300 W (LX300F, Japan) and LED lamps with 410–420 nm (GCH-4, Wuhan jiushang technology Co., Ltd.) are used for light irradiation. Electron spin resonance spectra (ESR) were collected with a JES-FA200 electron paramagnetic resonance spectrometer under visible-light irradiation.

2.2. Synthesis of MPor-Dha COFs

The cobalt *meso*-tetra(4-hydrazidocarbonylphenyl) porphyrin (CoPor, 22.4 mg) and 2, 5-dihydroxyterephthalaldehyde (Dha), 8 mg were charged into a Pyrex tube by mixed solvents of mesitylene (0.3 mL) and *N*-methyl-2-pyrrolidone (NMP, 0.7 mL) and 0.2 mL 6 M acetic acid (HOAc). The mixture was sonicated for a few minutes until the
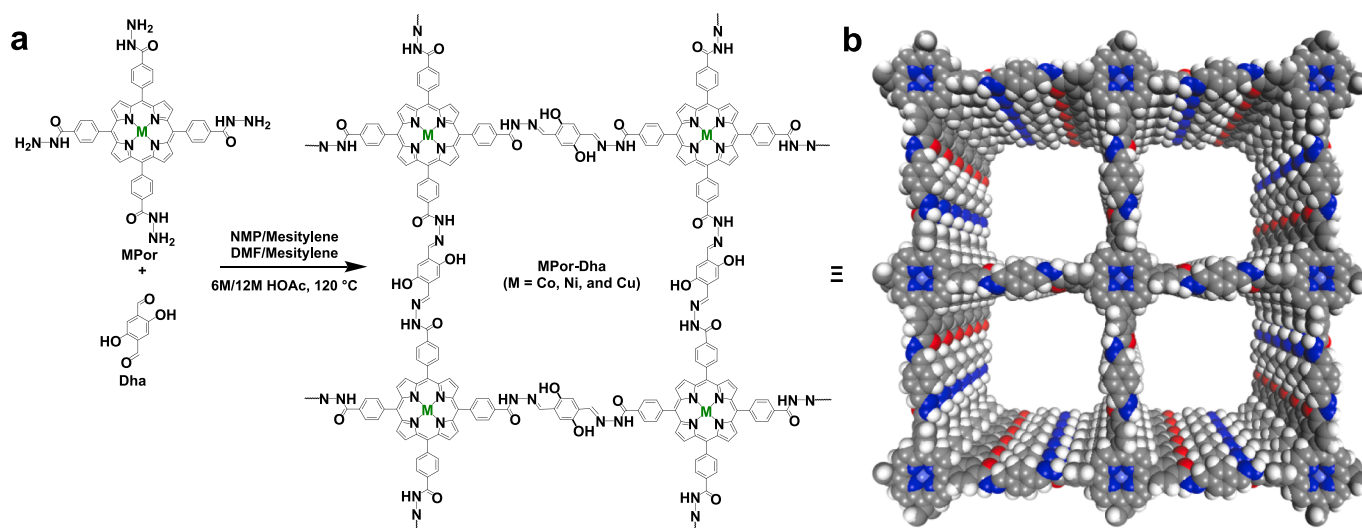

Fig. 1. (a) Synthetic scheme of 2D MPor-Dha COFs. (b) Space-filling model of MPor-Dha COFs.

monomers afforded homogeneous dispersions. Finally, the tube was evacuated to an internal pressure of 0.15 mmHg (liquid N$_2$ bath), and the tube was flame sealed. After sealing, the tube was heated at 120 °C for 3 days. After 3 days, the precipitate was collected by filtrations and washed with *N, N*-dimethylformamide (DMF), ethanol, and methanol to afford CoPor-Dha.

The nickel *meso*-tetra(4-hydrazidocarbonylphenyl) porphyrin (NiPor, 22.4 mg), copper *meso*-tetra(4-hydrazidocarbonylphenyl) porphyrin (CuPor, 22.6 mg), and Dha (8 mg) were charged into a Pyrex tube by adding DMF (0.7 mL), mesitylene (0.3 mL), and the mixture was sonicated for a few minutes till the monomers afford homogeneous dispersions. Then HOAc (12 M, 0.2 mL) was added. Finally, the tube was evacuated to an internal pressure of 0.15 mmHg (liquid N$_2$ bath), and the tube was flame sealed. After sealing, the reaction mixture of the tubes was heated at 120 °C for 3 days. The precipitate was separated by filtration and washed with DMF, anhydrous tetrahydrofuran, and methanol to afford the NiPor-Dha and CuPor-Dha, respectively.

2.3. General procedure for photocatalytic oxidation

2.3.1. Photocatalytic thioanisole oxidation

Typically, 0.05 mmol of thioanisole was added to the dispersion of COFs (10 mg) in 2 mL of acetonitrile (CH$_3$CN) and 1 mL of CH$_3$OH in a 10 mL reaction tube with a rubber septum. Three freeze–pump–thaw cycles filled the tube with oxygen before the reaction began. A light-emitting diode (LED) lamp was used to illuminate the reaction with visible light while being carried out at room temperature. In the quenching experiments, various scavengers at 50 mM were introduced to the scavenging tests while keeping other experimental parameters constant.

2.3.2. Photocatalytic hydroxylation of boronic acids

Typically, 0.1 mmol of phenyl boronic acids and 50 µL of triethylamine (TEA) were added after 10 mg of COFs were dispersed in 3 mL of CH$_3$CN in a 10 mL reaction tube with a rubber septum. Three freeze–pump–thaw cycles filled the tube with oxygen before the reaction began. A 300 W Xe lamp was used to illuminate the reaction with visible light while being carried out at room temperature. All the catalytic product yields were quantified by gas chromatography (GC), in which *N*-dodecane served as the internal standard for the GC analysis of the product yield. In the quenching experiments, various scavengers at 50 mM were introduced to the scavenging tests while keeping other experimental parameters constant.

3. Results and discussion

3.1. Synthesis and characterization.

The ligands used for the construction of COFs were synthesized using previous reports with modifications (Figs. S1–S4) [29,30]. The three metalloporphyrin COFs, denoted as CoPor-Dha, NiPor-Dha, and CuPor-Dha, were synthesized using solvothermal conditions in sealed tubes *via* the condensation of Dha with metalloporphyrin with Co, Ni, and Cu as metal centers, respectively (Fig. 1a). The synthetic conditions were
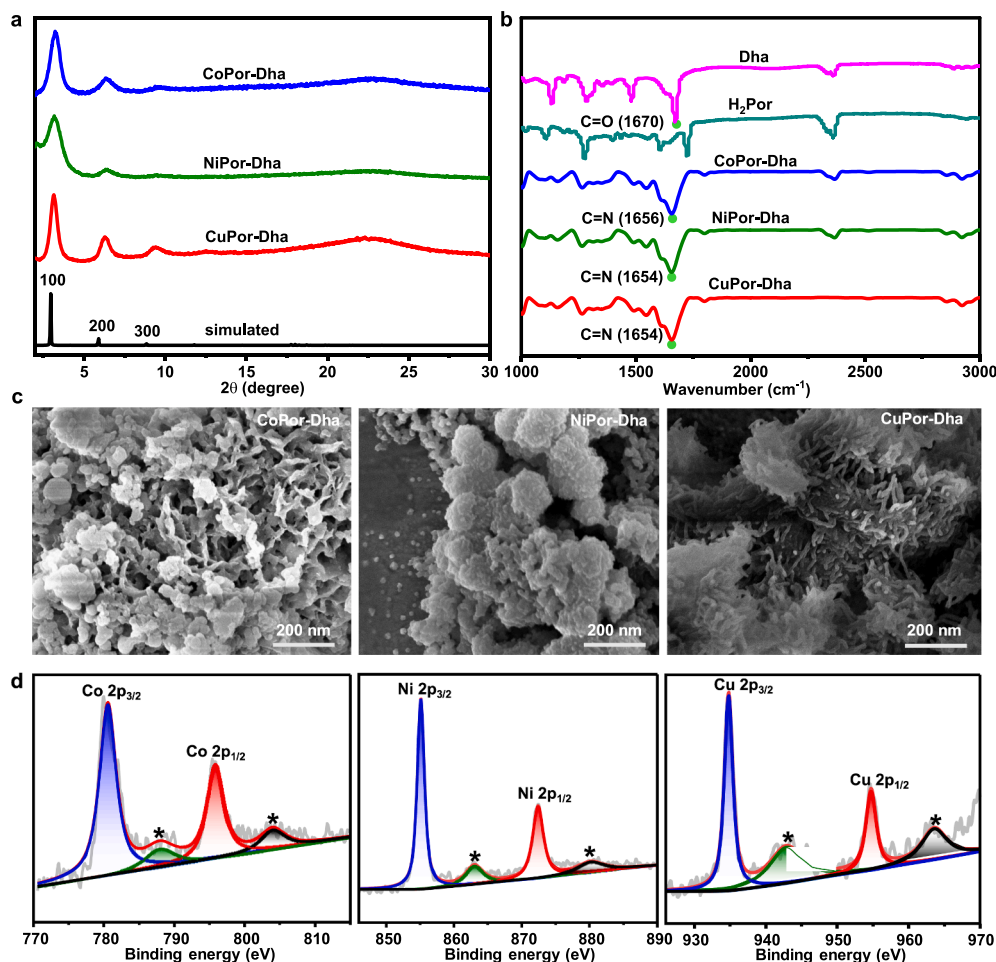

Fig. 2. (a) PXRD spectra of MPor-Dha COFs. (b) FTIR spectra of MPor-Dha COFs. (c) SEM images of MPor-Dha COFs. (d) High-resolution XPS spectra of metals in MPor-Dha COFs (* represents the satellite peaks).

optimized by changing the solvent system, reaction temperature, and reaction time. The optimal crystallinity of CoPor-Dha was obtained by using a mixed solvent of NMP and mesitylene (v/v = 7:3) at 120 °C, and NiPor-Dha and CuPor-Dha with the best crystallinity were observed by using DMF and mesitylene (v/v = 7:3) as the solvent at a reaction temperature of 120 °C.
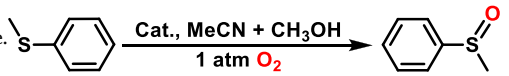
The highly crystalline nature of the three COFs has been confirmed by PXRD studies. The PXRD patterns of CoPor-Dha, NiPor-Dha, and CuPor-Dha exhibit a strong peak at 2.9° and two other prominent peaks at 5.8° and 8.8° (Fig. 2a, Fig. S5), which correspond to diffractions of (1 0 0), (2 0 0), and (3 0 0), respectively, indicating good long-range order along the *ab* plane. These PXRD patterns matched well with the the PXRD patterns of the powder-refined model with eclipsed packing mode. No residual peak indicative of the starting materials or other crystalline species was observed, indicating good phase purity (Fig. S6). The successful synthesis of the COFs is also supported by Fourier transform infrared (FT-IR) spectroscopy, which is illustrated by the disappearance of HC $=$ O stretching bands of Dha unit at 1670 cm^{-1} and the appearance of stretching vibrations of C $=$ N bands at 1654–1656 cm^{-1}, suggesting the effective formation of a hydrazone moiety (Fig. 2b). The porosity of the COFs was evaluated using nitrogen adsorption–desorption tests at 77 K. CoPor-Dha, NiPor-Dha, and CuPor-Dha demonstrate type-I isotherms for typical microporous materials (Fig. S7). The BET surface areas of CoPor-Dha, NiPor-Dha, and CuPor-Dha are determined to be 118, 150, and 286 m^2 g^{-1}, respectively. Scanning electron microscopy (SEM) images of the COF samples revealed the aggregated crystallites with irregular grains or fiber-shaped morphology (Fig. 2c). ICP–AES (Table S1) and XPS indicated that metal ions were successfully introduced into the porphyrin center. High-resolution XPS analysis was conducted to investigate the electronic state and composition of COFs. The XPS survey spectra suggested the presence of C, N, and the corresponding metal of Co, Ni, or Cu, consistent with the composition of the COFs (Fig. S8). In the deconvoluted high-resolution XPS spectra of Co, Ni, and Cu at 2p$_{1/2}$ and 2p$_{3/2}$ region, all show a single component with features of satellite peaks (Fig. 2d), implying that the metal ions in the three COFs have (+2) oxidation state [31,32]. Under an air atmosphere, TGA was conducted to determine the stability of MPor-Dha (Fig. S9).

3.2. Photocatalytic oxidation studies

In general, molecular oxygen can be photocatalytically activated to produce various ROS, such as $^1O_2$, $\bullet OH$, and $O_2^{\bullet -}$ [25,26,33–36]. The distinct capabilities of MPor-Dha in the production of $^1O_2$ and $O_2^{\bullet -}$ from O_2 under photoirradiation were tested by examining their behaviors in photocatalytic oxidation reactions.

The oxidation of thioanisole was first performed in CH$_3$CN under an O_2 environment with a blue LED light (410–420 nm) using MPor-Dha COFs as the photocatalysts. CoPor-Dha showed low catalytic activity with only a 7 % yield toward phenyl sulfoxide in 10 h (entry 1 in Table 1). NiPor-Dha gives a moderate yield of 15 % under the same conditions (entry 2 in Table 1). In sharp contrast, CuPor-Dha gives the highest catalytic activity with 82 % yield (entry 3 in Table 1). The

reaction is completely inhibited in the absence of the COF photocatalyst (entry 4 in Table 1) or in the N$_2$ atmosphere (entry 5 in Table 1), or in the absence of light (entry 6 in Table 1). The oxidation of thioanisole to phenyl sulfoxide is believed to be primarily $^1O_2$-engaged [26]. In our case, the generation of $^1O_2$ as the dominant ROS in the oxidation of thioanisole using CuPor-Dha is verified by scavenging experiments. As shown in Table S2, when the $^1O_2$ scavenger sodium azide (NaN$_3$) is added to the reaction mixtures, the reactions are completely inhibited. In contrast, with the addition of $O_2^{\bullet -}$ scavenger *p*-benzoquinone (*p*-BQ) and $\bullet OH$ scavenger (*t*-butanol), the reaction yields are minimally affected. The above experiments suggest that CuPor-Dha selectively facilitates the conversion of triplet to singlet excitons and exhibits the highest activity for $^1O_2$-mediated photooxidation of thioanisole to sulfoxide. On the contrary, CoPor-Dha, which gives a very low yield in the photooxidation of thioanisole, exhibits the lowest activity for $^1O_2$ generation.

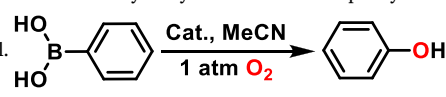Reaction conditions: catalyst (10 mg), thioanisole (0.05 mmol), 2 mL of CH$_3$CN, 1 mL of CH$_3$OH, blue LED light, O$_2$ (1 atm).[a] *N*-dodecane served as the internal standard for the GC. analysis of the product yield. [b] Under N$_2$. [c] Under O$_2$ and the absence of light.

Given the highest selectivity of CuPor-Dha in the generation of $^1O_2$, we further hypothesized that the other two MPor-Dha COFs (CoPor-Dha and NiPor-Dha) with different metal sites might be able to promote the formation of other types of ROS. We then explored the photocatalytic oxidation of phenylboronic acid to phenol, which is reported to be mainly mediated by $O_2^{\bullet -}$ [37–39]. To our delight, after 4 h of photo-irradiation with a 300 W Xe lamp, phenylboronic acid is efficiently oxidized into phenol in an excellent yield of 93 % with the use of CoPor-Dha (entry 1 in Table 2). In contrast, under the same conditions, NiPor-Dha gives a lower yield of 80 % for phenol (entry 2 in Table 2), and CuPor-Dha gives the lowest yield of 65 % (entry 3 in Table 2). In the absence of the COF photocatalyst (entry 4 in Table 2) or in the N$_2$ atmosphere (entry 5 in Table 2), or in the absence of light (entry 6 in Table 2), no product can be obtained. The oxidization of phenylboronic acid to phenol is predominantly mediated by $O_2^{\bullet -}$ as supported by scavenging experiments using CoPor-Dha. When the $O_2^{\bullet -}$ scavenger *p*-BQ is introduced to the reaction mixtures, the yield is suppressed significantly from 93 % to 23 % (entry 2 in Table S3). However, NaN$_3$ and *t*-butanol, scavengers for $^1O_2$ and $\bullet OH$, caused a slight decrease in yield (entries 1 and 3 in Table S3). These results suggest that CoPor-Dha, which is followed by NiPor-Dha and then CuPor-Dha, has the strongest tendency among the three COFs for promoting the dissociation of excitons to hot carriers under photoexcitation, showing the optimal activity for $O_2^{\bullet -}$-mediated phenylboronic acid oxidation to phenol.

Reaction conditions: catalyst (10 mg), phenylboronic acid (0.1 mmol), 3 mL of CH$_3$CN, 50 μL TEA, Xe lamp 300 W, O$_2$ (1 atm).[a] *N*-dodecane served as the internal standard for the GC. analysis of the product yield. [b] Under N$_2$. [c] Under O$_2$ and in the absence of light.

Our above results from the two photooxidative reactions, together with the quenching experiments, point to a metal-dependent trend in the regulated generation of $^1O_2$ and $O_2^{\bullet -}$ in which CoPor-Dha show the highest capability among the three COF in promoting the dissociation of

Table 1
Photocatalytic oxidation of thioanisole to methyl phenyl sulfoxide.

No.	catalyst	time (h)	yield (%) [a]
1	CoPor-Dha	10	7
2	NiPor-Dha	10	15
3	CuPor-Dha	10	82
4	blank	10	trace
5[b]	CuPor-Dha	10	trace
6[c]	CuPor-Dha	10	trace

Table 2
Photooxidative hydroxylation of phenylboronic acid to phenol.

No.	catalyst	time (h)	yield (%) [a]
1	CoPor-Dha	4	93
2	NiPor-Dha	4	80
3	CuPor-Dha	4	65
4	blank	4	trace
5[b]	CoPor-Dha	4	trace
6[c]	CoPor-Dha	4	trace

excitons into hot carriers, while CuPor-Dha shows preferentially transformation of triplet to singlet excitons. This regulated selectivity of the COFs in the generation of $^1O_2$ and $O_2^{\bullet-}$ is further supported by ESR spectroscopy with 5,5-dimethyl-1-pyrroline-*N*-oxide (DMPO) employed as a trapping compound for $O_2^{\bullet-}$. The ESR spectra show that the signal intensities of the three COFs are in the order CoPor-Dha > NiPor-Dha > CuPor-Dha, which is consistent with their capability in mediating the formation of $O_2^{\bullet-}$ (Fig. 3a). Further, 2,2,6,6-tetramethylpiperidine (TEMP) was also used as a trapping agent for $^1O_2$, resulting in the formation of the stable 2,2,6,6-tetramethylpiperidine oxide radical (TEMPO) upon its capture. Upon exposure to light irradiation, the CuPor-Dha exhibits strong and characteristic 1:1:1 triplet ESR signals of TEMPO, signifying the generation of $^1O_2$. Interestingly, the CoPor-Dha almost lack the corresponding signals. The order of relative signal intensities of TEMPO in the ESR spectra amongst the three COFs is CoPor-Dha < NiPor-Dha < CuPor-Dha, which aligns with their capability to facilitate the generation of $^1O_2$ (Fig. 3b).

3.3. Mechanism

It is usually speculated that the generation of $O_2^{\bullet-}$ involves an electron transfer process, in which $O_2^{\bullet-}$ is likely produced when the charge carriers that are formed around active metal centers upon light irritation migrate to the adsorbed O_2 [20]. Similar processes have been extensively investigated in semiconductor-based photocatalytic systems [40,41] for which the O_2 adsorption to the metal center is a prerequisite. In direct comparison, the formation of $^1O_2$ frequently involves energy transfer. Resonance energy transfer enables the triplet excitons to activate O_2 molecules in the ground state to $^1O_2$, during which oxygen can interact with catalysts through dipole–dipole interactions or charge exchange between donors and acceptors [42,43]. Given the above information, two essential criteria are usually considered for accessing whether an energy or electron transfer process will be induced between an excited semiconductor-based photocatalytic system and O_2 molecule [44]. The first one is the relative energy-level alignment of photocatalyst and O_2 which will direct the flow of charge carriers. The second is the binding affinity of the O_2 to the photocatalyst surface, which will affect the likelihood of the electron transfer process [43].

3.3.1. Band structure analysis

To disclose the distinct excitonic behavior of three COFs in regulating $^1O_2$ and $O_2^{\bullet-}$ generation, we first analyze the electronic property of

the COFs by conducting the light absorption spectra. All MPor-Dha COFs display broad light absorption extended to the near-infrared region, demonstrating their effective light harvesting capabilities ascribed to electron delocalization of MPor units (Figs. S10–S12). The bandgap energies for CoPor-Dha, NiPor-Dha, and CuPor-Dha are 1.82, 1.85, and 1.94 eV, respectively, as calculated from the corresponding Tauc plots (Fig. 4a-c). The Mott-Schottky plots were used to calculate the energy levels of the COFs (Fig. 4d-f). We found that center porphyrin metals have significant effect on the valency band (VB) and conduction band (CB) levels of the COFs. From Mott-Schottky plots, the CB levels of CoPor-Dha, NiPor-Dha, and CuPor-Dha are calculated as −1.17, −1.06, and −0.87 V vs the normal hydrogen electrode (NHE, pH = 6.8). Although the CB potential of these COFs is high enough for initiating many photocatalytic processes, e.g., the activation of O_2 ($E^0(O_2/O_2^{\bullet-})$ = −0.33 eV vs. NHE) [11], these varied CB levels could result in distinct paths for activating oxygen (Fig. S13). The CB energy levels of the three COFs follow the order of CoPor-Dha > NiPor-Dha > CuPor-Dha (Fig. S14). The more negative CB energy level of CoPor-Dha and NiPor-Dha suggests that the one-electron reduction of O_2 by the activated state of CoPor-Dha and NiPor-Dha will be more favorable than CuPor-Dha [45]. Instead, CuPor-Dha, with the lowest CB energy level, may facilitate the energy transfer process to a larger degree than the other two COFs. Meanwhile, CuPor-Dha with the lowest VB level which is corresponding to the hole with the highest oxidizing ability may also be able to promote the $^1O_2$ formation through the hole oxidation mechanism. Anodic photocurrent test also shows that under light irradiation CoPor-Dha has the highest photocurrent response, followed by NiPor-Dha and CuPor-Dha (Fig. S15), suggesting the same trend of charge transfer ability as band structure analysis [46].

3.3.2. DFT calculations

DFT calculations were then performed to determine the adsorption energy and the possible electron transfer between the COFs and O_2. The calculated results showed that the adsorption free energies (ΔG) between O_2 and CoPor-Dha, NiPor-Dha, and CuPor-Dha are −0.19 eV, 0.04 eV, and 0.39 eV, respectively (Fig. 5a). The most positive adsorption free energy of O_2 on CuPor-Dha suggests an unfavorable O_2 adsorption which is not beneficial for the electron transfer process, which is in-line with the lowest CB level of CuPor-Dha that leads to optimal selectivity of the energy transfer process for the generation of $^1O_2$. In contrast, the O_2 adsorption on CoPor-Dha and NiPor-Dha is more favorable than that on CuPor-Dha ($\Delta\Delta G$ = 0.58 eV, and 0.35 eV,
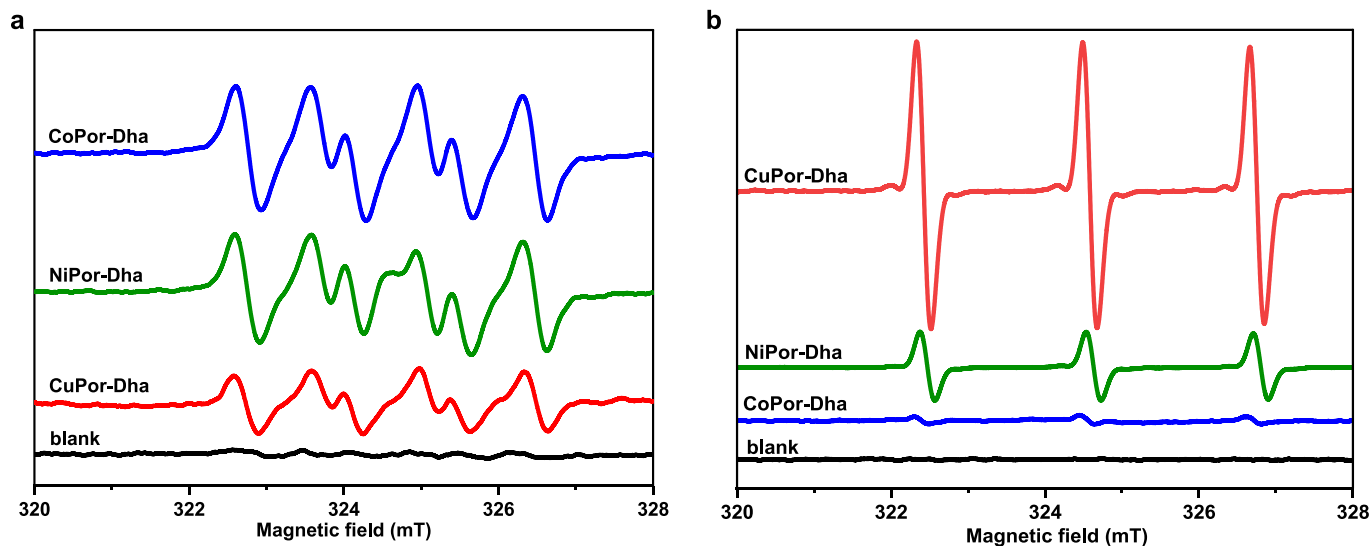
Fig. 3. ESR spectra of CoPor-Dha, NiPor-Dha, and CuPor-Dha in the presence of DMPO. (b) ESR spectra of CoPor-Dha, NiPor-Dha, and CuPor-Dha in the presence of TEMPO in an oxygen environment while exposed to visible light.
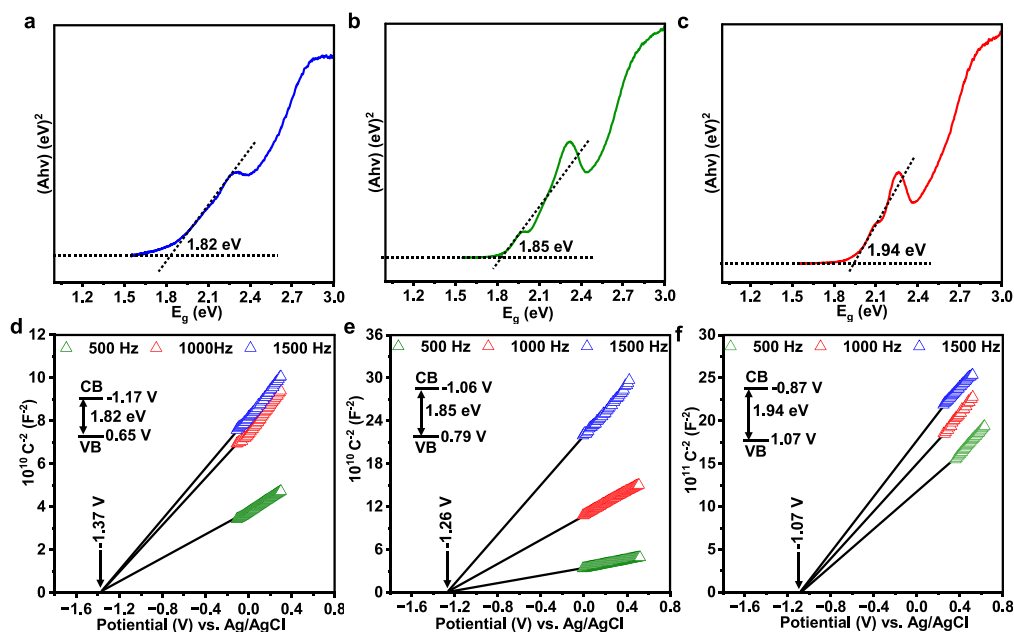
Fig. 4. Tauc plots of MPor-Dha (a) CoPor-Dha, (b) NiPor-Dha, and (c) CuPor-Dha. Mott-Schottky plots of (d) CoPor-Dha, (e) NiPor-Dha, and (f) CuPor-Dha in 0.1 M Na_2SO_4 aqueous solution. Inset: the energy diagram of the VB and CB levels of CoPor-Dha, NiPor-Dha, and CuPor-Dha.
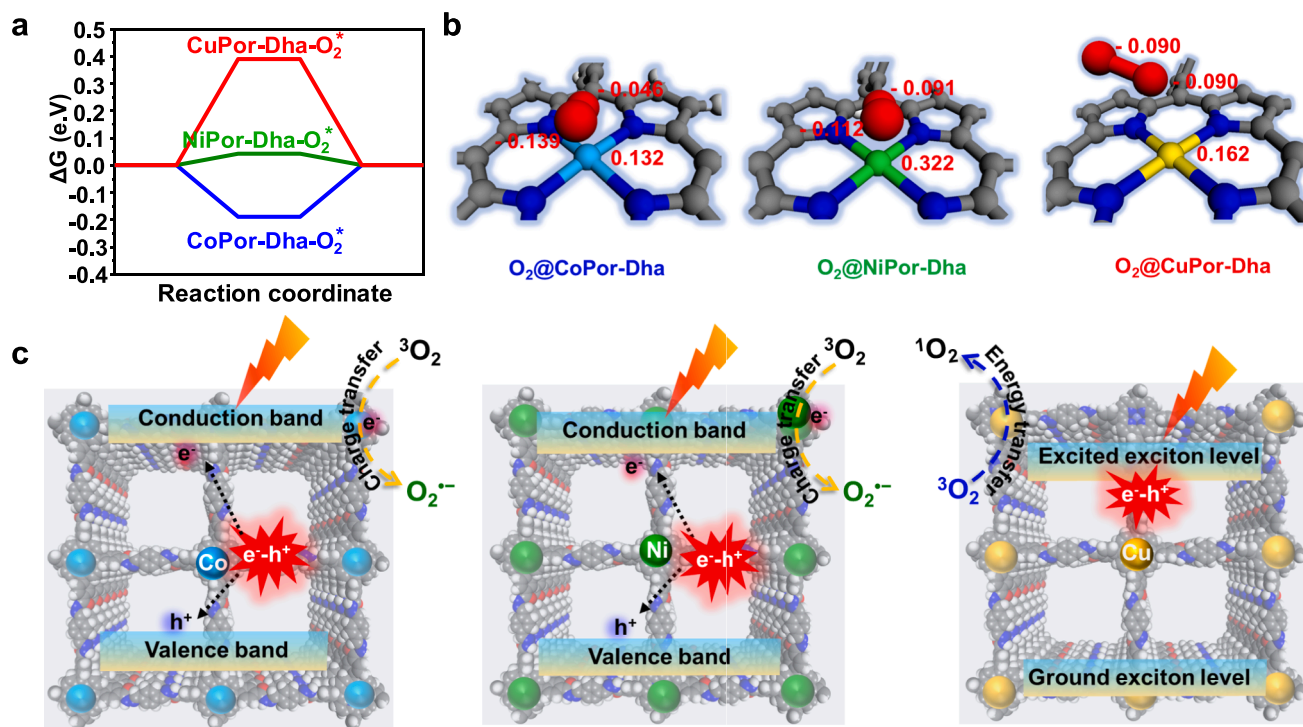

Fig. 5. (a) Free energy profile for the adsorption of oxygen molecules onto metal sites in MPor-Dha. (b) Calculated Mulliken charges for metal centers of CoPor-Dha, NiPor-Dha, and CuPor-Dha and oxygen atoms upon O_2 adsorption. (c) Schemes of photocatalytic activation of molecular oxygen on CoPor-Dha, NiPor-Dha, and CuPor-Dha.

respectively). From the calculated adsorption free energies, the O_2 adsorption on CoPor-Dha is more favorable than NiPor-Dha. Combined with its suitable CB energy level, the electron transfer process may be more favored for the exciton in CoPor-Dha than that in NiPor-Dha, leading to the highest selectivity for $O_2^{\bullet-}$ generation. Consequently, the computed Mulliken charges for the metal center of CoPor-Dha, NiPor-Dha, and CuPor-Dha upon O_2 adsorption are 0.132, 0.322, and 0.162, respectively (Fig. 5a). Additionally, the Mulliken charges on the absorbed O_2 over CoPor-Dha, NiPor-Dha, and CuPor-Dha are respectively −0.184, −0.203, and −0.180. These results also supported a larger degree of electron transfer to O_2 from CoPor-Dha and NiPor-Dha compared to CuPor-Dha (Fig. 5b). Therefore, the observed modulated excitonic behavior of three COFs in the regulated generation of $^1O_2$ and $O_2^{\bullet-}$ (Fig. 5c) is likely ascribed to a combined effect of their band structure and binding affinity to O_2 that originates from the identity of the metal center.

4. Conclusions

In conclusion, the regulated production of two major ROS, $^1O_2$ and $O_2^{\bullet-}$, was successfully achieved using a three-membered COF array constructed of metalloporphyrin cores with embedded center metal ions from the first-row transition metals. The regulated production of $^1O_2$ and $O_2^{\bullet-}$ has resulted in the distinct performance of the three COFs in photocatalytic aerobic oxidations. The COF-incorporated cobalt porphyrin exhibited the highest activity of the COF array in $O_2^{\bullet-}$-mediated oxidation. The copper porphyrin-based COF shows the best activity in promoting $^1O_2$ generation. Electronic property study and DFT calculation show that the distinct excitonic behavior of three COFs in regulated $^1O_2$ and $O_2^{\bullet-}$ generation can be explained by their different band levels and O_2 adsorption ability that influence the energy and charge transfer process between O_2 and the COFs. Our work presents a compelling and modular approach for controlling ROS production for efficient photocatalytic performance, which is supposed to find broad applications based on ROS-involved oxidation reactions.

5. Authorship contribution statement

H.L.J. and Z.M. conceived the idea and supervised the project. S.S. carried out the synthesis, characterization, and catalysis experiments. Z. M. and S.S. wrote the manuscript. X.G. performed the interpretation of the results and data analysis. Y.Z. conducted the reproducibility of the results. Onder Metin edited the manuscript and provided useful comments. All authors discussed the results and commented on the paper.

Declaration of Competing Interest

The authors declare that they have no known competing financial interests or personal relationships that could have appeared to influence the work reported in this paper.

Data availability

Data will be made available on request.

Acknowledgements

Appendix A. Supplementary data

Supplementary data to this article can be found online at https://doi.org/10.1016/j.cej.2023.146623.

References

[1] A.A. Ghogare, A. Greer, Using singlet oxygen to synthesize natural products and drugs, Chem. Rev. 116 (2016) 9994–10034, https://doi.org/10.1021/acs.chemrev.5b00726.
[2] A. Sagadevan, K.C. Hwang, M.-D. Su, Singlet oxygen-mediated selective C-H bond hydroperoxidation of ethereal hydrocarbons, Nat. Commun. 8 (2017) 1812, https://doi.org/10.1038/s41467-017-01906-5.
[3] R. Chen, J.-L. Shi, Y. Ma, G. Lin, X. Lang, C. Wang, Designed synthesis of a 2D porphyrin-based sp² carbon-conjugated covalent organic framework for heterogeneous photocatalysis, Angew. Chem. Int. Ed. 58 (2019) 6430–6434, https://doi.org/10.1002/anie.201902543.
[4] S. Gligorovski, R. Strekowski, S. Barbati, D. Vione, Environmental implications of hydroxyl radicals (•OH), Chem. Rev. 115 (2015) 13051–13092, https://doi.org/10.1021/cr500310b.
[5] E.C. Wert, F.L. Rosario-Ortiz, D.D. Drury, S.A. Snyder, Formation of oxidation byproducts from ozonation of wastewater, Water Res. 41 (2007) 1481–1490, https://doi.org/10.1016/j.watres.2007.01.020.
[6] X. Li, N. Kwon, T. Guo, Z. Liu, J. Yoon, Innovative strategies for hypoxic-tumor photodynamic therapy, Angew. Chem. Int. Ed. 57 (2018) 11522–11531, https://doi.org/10.1002/anie.201805138.
[7] T.J. Dougherty, C.J. Gomer, B.W. Henderson, G. Jori, D. Kessel, M. Korbelik, J. Moan, Q. Peng, Photodynamic therapy, J. Natl Cancer Inst. 90 (1998) 889–905, https://doi.org/10.1093/jnci/90.12.889.
[8] A.P. Castano, T.N. Demidova, M.R. Hamblin, Mechanisms in photodynamic therapy: part one—photosensitizers, photochemistry and cellular localization, Photodiagn. Photodyn. Ther. 1 (2004) 279–293, https://doi.org/10.1016/S1572-1000(05)00007-4.
[9] J. Ji, Q. Yan, P. Yin, S. Mine, M. Matsuoka, M. Xing, Defects on CoS$_{2-x}$: Tuning redox reactions for sustainable degradation of organic pollutants, Angew. Chem. Int. Ed. 60 (2021) 2903–2908, https://doi.org/10.1002/anie.202013015.
[10] H. Wang, S. Chen, D. Yong, X. Zhang, S. Li, W. Shao, X. Sun, B. Pan, Y. Xie, Giant electron–hole interactions in confined layered structures for molecular oxygen activation, J. Am. Chem. Soc. 139 (2017) 4737–4742, https://doi.org/10.1021/jacs.6b12273.
[11] Y. Nosaka, A.Y. Nosaka, Generation and detection of reactive oxygen species in photocatalysis, Chem. Rev. 117 (2017) 11302–11336, https://doi.org/10.1021/acs.chemrev.7b00161.
[12] M.C. DeRosa, R.J. Crutchley, Photosensitized singlet oxygen and its applications, Coord. Chem. Rev. 233 (2002) 351–371.
[13] I. Kumar, R. Kumar, S.S. Gupta, U. Sharma, C$_{70}$ fullerene catalyzed photoinduced aerobic oxidation of benzylamines to imines and aldehydes, J. Org. Chem. 86 (2021) 6449–6457, https://doi.org/10.1021/acs.joc.1c00297.
[14] C.B. Ong, L.Y. Ng, A.W. Mohammad, A review of ZnO nanoparticles as solar photocatalysts: Synthesis, mechanisms and applications, Renew. Sustain. Energy Rev. 81 (2018) 536–551, https://doi.org/10.1016/j.rser.2017.08.020.
[15] S. Furukawa, Y. Ohno, T. Shishido, K. Teramura, T. Tanaka, Selective amine oxidation Using Nb$_2$O$_5$ photocatalyst and O$_2$, ACS Catal. 1 (2011) 1150–1153, https://doi.org/10.1021/cs200318n.
[16] A.K. Simlandy, B. Bhattacharyya, A. Pandey, S. Mukherjee, Picosecond electron transfer from quantum dots enables a general and efficient aerobic oxidation of boronic acids, ACS Catal. 8 (2018) 5206–5211, https://doi.org/10.1021/acscatal.8b01078.
[17] C. Shang, Z.-P. Liu, Origin and activity of gold nanoparticles as aerobic oxidation catalysts in aqueous solution, J. Am. Chem. Soc. 133 (2011) 9938–9947, https://doi.org/10.1021/ja203468v.
[18] A. Gellé, T. Jin, L. de la Garza, G.D. Price, L.V. Besteiro, A. Moores, Applications of plasmon-enhanced nanocatalysis to organic transformations, Chem. Rev. 120 (2020) 986–1041, https://doi.org/10.1021/acs.chemrev.9b00187.
[19] H. Wang, S. Jiang, S. Chen, X. Zhang, W. Shao, X. Sun, Z. Zhao, Q. Zhang, Y. Luo, Y. Xie, Insights into the excitonic processes in polymeric photocatalysts, Chem. Sci. 8 (2017) 4087–4092, https://doi.org/10.1039/C7SC00307B.
[20] H. Wang, X. Sun, D. Li, X. Zhang, S. Chen, W. Shao, Y. Tian, Y. Xie, Boosting hot-electron generation: exciton dissociation at the order–disorder interfaces in polymeric photocatalysts, J. Am. Chem. Soc. 139 (2017) 2468–2473, https://doi.org/10.1021/jacs.6b12878.
[21] A. Naim, Y. Chevalier, Y. Bouzidi, P. Gairola, P. Mialane, A. Dolbecq, F. Avenier, J.-P. Mahy, Aerobic oxidation catalyzed by polyoxometalates associated to an artificial reductase at room temperature and in water, Inorg. Chem. Front. 7 (2020) 2362–2369, https://doi.org/10.1039/D0QI00442A.
[22] J. Ding, W. Xu, H. Wan, D. Yuan, C. Chen, L. Wang, G. Guan, W.-L. Dai, Nitrogen vacancy engineered graphitic C$_3$N$_4$-based polymers for photocatalytic oxidation of aromatic alcohols to aldehydes, Appl. Catal. B 221 (2018) 626–634, https://doi.org/10.1016/j.apcatb.2017.09.048.
[23] Y. Chen, X. Luo, J. Zhang, L. Hu, T. Xu, W. Li, L. Chen, M. Shen, S.-B. Ren, D.-M. Han, G.-H. Ning, D. Li, Bandgap engineering of covalent organic frameworks for boosting photocatalytic hydrogen evolution from water, J. Mater. Chem. A 10 (2022) 24620–24627, https://doi.org/10.1039/D2TA07271H.
[24] J. Guo, D. Jiang, Covalent organic frameworks for heterogeneous catalysis: principle, current status, and challenges, ACS Cent. Sci. 6 (2020) 869–879, https://doi.org/10.1021/acscentsci.0c00463.
[25] Y. Meng, Y. Luo, J.-L. Shi, H. Ding, X. Lang, W. Chen, A. Zheng, J. Sun, C. Wang, 2D and 3D porphyrinic covalent organic frameworks: The influence of dimensionality on functionality, Angew. Chem. Int. Ed. 59 (2020) 3624–3629, https://doi.org/10.1002/anie.201913091.
[26] Y.-Z. Chen, Z.U. Wang, H. Wang, J. Lu, S.-H. Yu, H.-L. Jiang, Singlet oxygen-engaged selective photo-oxidation over Pt nanocrystals/porphyrinic MOF: The roles of photothermal effect and Pt electronic state, J. Am. Chem. Soc. 139 (2017) 2035–2044, https://doi.org/10.1021/jacs.6b12074.
[27] S. Wu, Y.-F. Zhang, H. Ding, X. Li, X. Lang, Hydrazone-linked 2D porphyrinic covalent organic framework photocatalysis for visible light-driven aerobic oxidation of amines to imines, J. Colloid Interface Sci. 610 (2022) 446–454.
[28] Y. Qian, D. Li, Y. Han, H.-L. Jiang, Photocatalytic molecular oxygen activation by regulating excitonic effects in covalent organic frameworks, J. Am. Chem. Soc. 142 (2020) 20763–20771, https://doi.org/10.1021/jacs.0c09727.
[29] M.O. Cichocka, Z. Liang, D. Feng, S. Back, S. Siahrostami, X. Wang, L. Samperisi, Y. Sun, H. Xu, N. Hedin, H. Zheng, X. Zou, H.-C. Zhou, Z. Huang, A porphyrinic zirconium metal–organic framework for oxygen reduction reaction: Tailoring the spacing between active-sites through chain-based inorganic building units, J. Am. Chem. Soc. 142 (2020) 15386–15395, https://doi.org/10.1021/jacs.0c06329.

[30] W. Zhang, P. Jiang, Y. Wang, J. Zhang, P. Zhang, Bottom-up approach to engineer two covalent porphyrinic frameworks as effective catalysts for selective oxidation, Catal. Sci. Technol. 5 (2015) 101–104, https://doi.org/10.1039/C4CY00969J.

[31] H.-J. Zhu, M. Lu, Y.-R. Wang, S.-J. Yao, M. Zhang, Y.-H. Kan, J. Liu, Y. Chen, S.-L. Li, Y.-Q. Lan, Efficient electron transmission in covalent organic framework nanosheets for highly active electrocatalytic carbon dioxide reduction, Nat. Commun. 11 (2020) 497, https://doi.org/10.1038/s41467-019-14237-4.

[32] H. Ding, Y.-R. Wang, M. Liu, J.-W. Shi, T.-Y. Yu, Y.-S. Xia, M. Lu, Y.-L. Yang, Y. Chen, S.-L. Li, Y.-Q. Lan, Electronic tuning of active sites in bifunctional covalent organic frameworks for photoassisted CO$_2$ electrocatalytic full reaction, Chem. Mater. 34 (2022) 10752–10760, https://doi.org/10.1021/acs.chemmater.2c02962.

[33] P.-F. Wei, M.-Z. Qi, Z.-P. Wang, S.-Y. Ding, W. Yu, Q. Liu, L.-K. Wang, H.-Z. Wang, W.-K. An, W. Wang, Benzoxazole-linked ultrastable covalent organic frameworks for photocatalysis, J. Am. Chem. Soc. 140 (2018) 4623–4631, https://doi.org/10.1021/jacs.8b00571.

[34] C. Xu, Y. Pan, G. Wan, H. Liu, L. Wang, H. Zhou, S.-H. Yu, H.-L. Jiang, Turning on visible-light photocatalytic C−H oxidation over metal–organic frameworks by introducing metal-to-cluster charge transfer, J. Am. Chem. Soc. 141 (2019) 19110–19117, https://doi.org/10.1021/jacs.9b09954.

[35] S. Li, L. Li, Y. Li, L. Dai, C. Liu, Y. Liu, J. Li, J. Lv, P. Li, B. Wang, Fully conjugated donor–acceptor covalent organic frameworks for photocatalytic oxidative amine coupling and thioamide cyclization, ACS Catal. 10 (2020) 8717–8726, https://doi.org/10.1021/acscatal.0c01242.

[36] C. Xu, H. Liu, D. Li, J.-H. Su, H.-L. Jiang, Direct evidence of charge separation in a metal–organic framework: efficient and selective photocatalytic oxidative coupling of amines via charge and energy transfer, Chem. Sci. 9 (2018) 3152–3158, https://doi.org/10.1039/C7SC05296K.

[37] S. Bi, P. Thiruvengadam, S. Wei, W. Zhang, F. Zhang, L. Gao, J. Xu, D. Wu, J.-S. Chen, F. Zhang, Vinylene-bridged two-dimensional covalent organic frameworks via knoevenagel condensation of tricyanomesitylene, J. Am. Chem. Soc. 142 (2020) 11893–11900, https://doi.org/10.1021/jacs.0c04594.

[38] S.P. Pitre, C.D. McTiernan, H. Ismaili, J.C. Scaiano, Mechanistic insights and kinetic analysis for the oxidative hydroxylation of arylboronic acids by visible light photoredox catalysis: A metal-free alternative, J. Am. Chem. Soc. 135 (2013) 13286–13289, https://doi.org/10.1021/ja406311g.

[39] J.A. Johnson, J. Luo, X. Zhang, Y.-S. Chen, M.D. Morton, E. Echeverría, F.E. Torres, J. Zhang, Porphyrin-metalation-mediated tuning of photoredox catalytic properties in metal–organic frameworks, ACS Catal. 5 (2015) 5283–5291, https://doi.org/10.1021/acscatal.5b00941.

[40] R. Li, Y. Weng, X. Zhou, X. Wang, Y. Mi, R. Chong, H. Han, C. Li, Achieving overall water splitting using titanium dioxide-based photocatalysts of different phases, Energ. Environ. Sci. 8 (2015) 2377–2382, https://doi.org/10.1039/C5EE01398D.

[41] P. Zhang, Y. Tong, Y. Liu, J.J.M. Vequizo, H. Sun, C. Yang, A. Yamakata, F. Fan, W. Lin, X. Wang, W. Choi, Heteroatom dopants promote two-electron O$_2$ reduction for photocatalytic production of H$_2$O$_2$ on polymeric carbon nitride, Angew. Chem. Int. Ed. 59 (2020) 16209–16217, https://doi.org/10.1002/anie.202006747.

[42] L. Cao, Z. Lin, W. Shi, Z. Wang, C. Zhang, X. Hu, C. Wang, W. Lin, Exciton migration and amplified quenching on two-dimensional metal–organic layers, J. Am. Chem. Soc. 139 (2017) 7020–7029, https://doi.org/10.1021/jacs.7b02470.

[43] R. Haldar, M. Jakoby, A. Mazel, Q. Zhang, A. Welle, T. Mohamed, P. Krolla, W. Wenzel, S. Diring, F. Odobel, B.S. Richards, I.A. Howard, C. Wöll, Anisotropic energy transfer in crystalline chromophore assemblies, Nat. Commun. 9 (2018) 4332, https://doi.org/10.1038/s41467-018-06829-3.

[44] J.T. DuBose, P.V. Kamat, Energy versus electron transfer: Managing excited-state interactions in perovskite nanocrystal–molecular hybrids, Chem. Rev. 122 (2022) 12475–12494, https://doi.org/10.1021/acs.chemrev.2c00172.

[45] C. Yu, J. He, M. Tan, Y. Hou, H. Zeng, C. Liu, H. Meng, Y. Su, L. Qiao, T. Lookman, Y. Bai, Selective enhancement of photo-piezocatalytic performance in BaTiO$_3$ Via heterovalent ion doping, Adv. Funct. Mater. 32 (2022) 2209365, https://doi.org/10.1002/adfm.202209365.

[46] A. Podborska, M. Suchecki, K. Mech, M. Marzec, K. Pilarczyk, K. Szaciłowski, Light intensity-induced photocurrent switching effect, Nat. Commun. 11 (2020) 854, https://doi.org/10.1038/s41467-020-14675-5.